Materials Today Sustainability 31 (2025) 101155

Contents lists available at ScienceDirect

Materials Today Sustainability

journal homepage: www.journals.elsevier.com/materials-today-sustainability

Stainless steel 316L as bipolar plate material in proton exchange membrane water electrolyzer: The influence of potential and temperature on dissolution stability

Lena Fiedler [a,b,*], Tien-Ching Ma [a,b], Birk Fritsch [a], Martin Dierner [c], Darius Hoffmeister [a,b], Carmen Rubach [c], Johannes Will [c], Thomas Przybilla [c], Erdmann Spiecker [c], Dominik Dworschak [a], Karl J.J. Mayrhofer [a], Andreas Hutzler [a,**]

[a] Forschungszentrum Jülich GmbH, Helmholtz Institute Erlangen-Nürnberg for Renewable Energy (IET-2), Cauerstraße 1, 91058, Erlangen, Germany[1]
[b] Department of Chemical and Biological Engineering, Friedrich-Alexander-Universität Erlangen-Nürnberg, Egerlandstraße 3, 91058, Erlangen, Germany
[c] Institute of Micro- and Nanostructure Research (IMN) & Center for Nanoanalysis and Electron Microscopy (CENEM), Interdisciplinary Center for Nanostructured Films (IZNF), Friedrich-Alexander-Universität Erlangen-Nurnberg, 91058, Erlangen, Germany

ARTICLE INFO

Keywords:
Water splitting
Stainless steel
Corrosion
Bipolar plates
DI water
H_2SO_4

ABSTRACT

Stainless steel is a possible candidate for replacing titanium-based bipolar plates to reduce the cost of proton exchange membrane water electrolyzers. However, stainless steel is suspected to dissolve which could harm the system. Herein, we investigate the influence of applied potentials and temperatures on the dissolution stability of stainless steel (316L) in deionized (DI) water (pH ≈ 7) and highly diluted H_2SO_4 (pH ≈ 3) utilizing a scanning flow cell coupled on-line to an inductively coupled plasma mass spectrometer (SFC-ICP-MS). In H_2SO_4, the applied potentials critically influence the dissolution rates of 316L. Detrimental dissolution is observed at the open circuit potential, whereas dissolution is minimal in a potential window between 0.76 and 0.96 V. Temperature enhances the dissolution of 316L, especially due to a reduced stability of Cr. In DI water, the stability of 316L remains widely independent of potential and temperature, with dissolution rates remaining at an overall low level. Complementary scanning- and transmission electron microscopy reveal corrosion phenomena after electrochemical measurements in pH 3. Our results provide insights into factors influencing the stability of 316L and emphasize the importance of testing conditions that accurately mimic real-operations.

1. Introduction

Defossilisation is one of the major challenges for our society. Achieving that goal requires tons of green hydrogen to replace hydrogen from fossil sources (e.g. gray hydrogen) in industry and mobility or replace coal in steel production [1]. Germany alone is estimated to require between 95 and 130 TWh of green hydrogen in 2030 [2]. However, at the end of 2023, only 1.4 GW electrolyzer capacity was achieved worldwide [3], and the costs of green hydrogen are not yet competitive [4]. Green hydrogen is produced by splitting water into hydrogen and oxygen by power from renewable energies – the so-called electrolysis process. Besides the well-established alkaline water electrolysis, the other commercially available electrolysis technique, proton exchange membrane water electrolysis (PEMWE), is advantageous when coupled to renewable energies due to the possibility of reaching high current densities with a fast response upon changes in the power input [5,6]. Here, the high costs of the produced hydrogen are caused by the need for expensive materials due to the acidic environment paired with high temperatures and potentials.

Therefore, much research focuses on replacing or lowering the usage of iridium, applied as anode catalyst, due to its very high cost and scarcity, while increasing its utilization [7–11]. Less in focus, yet one of

This article is part of a special issue entitled: Sustainable H2 Fuel published in Materials Today Sustainability.

* Corresponding author. Forschungszentrum Jülich GmbH, Helmholtz Institute Erlangen-Nürnberg for Renewable Energy (IET-2), Cauerstraße 1, 91058, Erlangen, Germany.
** Corresponding author.
E-mail addresses: l.fiedler@fz-juelich.de (L. Fiedler), a.hutzler@fz-juelich.de (A. Hutzler).
[1] Homepage: http://www.hi-ern.de/en

https://doi.org/10.1016/j.mtsust.2025.101155
Received 31 January 2025; Received in revised form 11 April 2025; Accepted 9 June 2025
Available online 11 June 2025

the major cost factors of the stack components, are bipolar plates (BPP) [12]. The BPPs separate the single cells from each other, distribute water and product gases, and conduct heat and current [13]. The state-of-the-art material is titanium, often coated with noble metals to lower contact resistances [14]. Replacing titanium with an alternative material is, however, not straightforward as there are many requirements for a BPP: offering a high thermal and electrical conductivity with a low interfacial contact resistance (ICR) to the adjoining porous transport layer (PTL) while being corrosion-resistant, especially against harsh conditions at the anode side [13].

A possible alternative material is austenitic stainless steel. Its main advantages are the lower costs, not only of the material itself but also of its processing [15]. Besides, other metals are tested as BPP materials, for example, niobium, tantalum, or copper [16,17]. Moreover, new results indicate the possibility of using carbon-based or carbon-coated stainless steel BPPs. Yet, this research is still fundamental, and these materials are not yet ready for competitive incorporation into PEMWE systems. For example, carbon-based BPPs exhibit a remarkable stability in single cell tests for more than 567 h, however with lower performance compared to a Ti-BPP [18]. A possible explanation could be either a much higher, near-neutral pH value or lower potentials at the BPP. To the best of our knowledge, no *in situ* pH measurement is reported in the literature yet, but measurements in the feed water tanks hint at a slightly acidic, near-neutral pH value in close proximity to the BPP [19,20]. A highly acidic pH was often assumed for *ex situ* testing, while other tests were performed at near-neutral pH values [16,17,21–23]. Moreover, recent findings suggest potentials that are close to the open circuit potential (OCP) at the anode bipolar plate at sufficient distances from the anode catalyst layer due to a decoupling by the low ionic conductivity of the feed deionized (DI) water [20,24]. However, other researchers mention the corrosion of non-coated stainless steel BPPs in single cell tests, stating the indication of dissolution and thereby higher potentials at the BPP [25]. Jung et al. [26] used a carbon-based BPP in a unitized regenerative fuel cell and observed high corrosion after usage in electrolysis mode. Remarkably, even for a Ti-BPP, a relatively corrosion-resistant material, degradation was reported after single cell tests [27].

Herein, we focus on the utilization of stainless steel, namely 316L, as BPP material. Compared to pure carbon-based materials the usage of metallic BPPs offers certain advantages: higher mechanical strength, facile fabrication, and higher possible production rates as known from the fuel cell industry [28–30]. In general, it is assumed that metallic BPPs must be coated for two main reasons: first, to prevent the dissolution of the base material, and second, to prevent the formation of a passivating, non-conductive oxide layer that increases the ICR (for example the formation of TiO_2 on Ti BPPs). Therefore coatings such as Ti/Pt [21,31], Ti/Nb [32–34], Nb [33], and Ti/Au [35] are extensively tested in literature.

Unprotected stainless steel is suspected of corroding under assumed conditions in an electrolyzer, leading to the leaching of metal cations, mainly Fe, Ni, and Cr, the main alloy components of stainless steel. These cations are known to harm an electrolyzer by membrane or catalyst layer poisoning or deterioration [36–40]. *Ex situ* corrosion measurements showed corrosion and dissolution of stainless steel, however, measured at rather simulated conditions (at pH 5.5 with unknown H_2SO_4/NaOH concentration and 5 ppm HF or at pH 5.5 with 0.1 mM H_2SO_4 and 0.1 M Na_2SO_4 or in 1 mM H_2SO_4 + 0.1 mM HF, respectively.) [16,22,25] For more realistic testing conditions, we developed a setup based on the well-established scanning flow cell (SFC), a system similar to atomic emission spectroelectrochemistry (AESEC) that however allows scanning across the sample [41–44]. To enable testing in low-conducting electrolytes, we decreased the distance between working, reference, and counter electrode, even enabling measurements in DI water [40]. On-line coupling of the SFC to an inductively coupled plasma mass spectrometer (ICP-MS) allows the direct, time- and potential-resolved detection of any dissolved metal from the sample. Compared to the coupling with an atomic emission spectrometer as in AESEC, coupling with an ICP-MS offers superior detection limits but lower matrix tolerance [44]. We showed that 316L dissolves in DI water and highly-diluted H_2SO_4 upon polarization. However, a rough approximation from the *ex situ* measurements to the single cell level suggested that the impact on a single cell might be much lower than expected [40].

In this study, we investigate the stability of bare stainless steel (type 316L) more extensively. First, we examine the influence of the applied potentials from the OCP-value up to 2 V at a sample temperature of 60 °C. Second, we study the fundamental influence of the temperature on the dissolution of 316L. Both investigations are performed in DI water with a pH of approximately 7 and in highly diluted sulfuric acid (0.5 mM, pH ≈ 3) to simulate application-near conditions. Our results shine light on the dissolution of 316L, providing insights about dissolution and indicating under which conditions coatings of steel components might be necessary.

2. Experimental section

2.1. Materials

316L (d = 1 mm) was purchased from Hans-Erich-Gemmel & Co GmbH. On the day before measurements, the sample was ground with sandpaper (from P240 to P4000, Struers) and then polished with 3 μm diamond paste (MD-Mol, Struers) with a semi-automatic polishing machine (Struers, LapoPol-30 with LaboForce 100). The samples were cleaned with isopropanol and water before and after sonication in DI water (2 × 10 min). The polished samples were stored in ambient air until the measurement.

For the EBSD measurements, the sample was ground manually with sandpaper (P1200 to P2400, Struers) followed by polishing with 6, 3, and 1 μm diamond paste (Meta Di II, Buehler) and 0.04 μm colloidal silica suspension (Allied).

2.2. Electrochemical and stability measurements (SFC-ICP-MS)

All electrochemical measurements were performed using a scanning flow cell coupled on-line to an inductively coupled plasma mass spectrometer (SFC-ICP-MS) that enables the time-resolved detection of dissolved species from the sample into the electrolyte. A detailed description of the setup can be found elsewhere [40]. In short, the electrolyte is pumped constantly through the V-shaped channels of the SFC and fed into an ICP-MS (flow rate measured daily). At the channels's apex, the SFC has an elliptical opening (A = 3.63 mm^2) to contact the working electrode (WE). A glassy carbon rod (Ø = 1.6 mm, HTW Hochtemperatur-Werkstoffe) placed at the inlet and a leakage-free Ag|AgCl-reference electrode (LF-1.6-48, Ø = 1.6 mm, Innovative Instruments, Inc.) placed at the outlet, were used as counter (CE) and reference electrode (RE), respectively. As the RE is leakage-free, we exclude any corrosion enhancing influence of Cl^-. A potentiostat (Reference 620, Gamry Instruments) was used and the sample was placed on a temperature-controlled stage to heat the sample to the desired measurement temperature (T_{stage}). Either Ar-purged DI water or Ar-purged 0.5 mM H_2SO_4 (Ultrex® II, J.T.Baker, diluted with ultrapure water (18.2 MΩ cm^{-1})) was used as electrolyte. The pH value of the Ar-purged DI water is ≈7, the one of 0.5 mM H_2SO_4 ≈3 (measured with a calibrated pH meter (HI5521-Benchmeter, Hanna Instruments)). The influence of purging the electrolyte with O_2 instead of Ar, as we focus on the anode side of a PEMWE, is shown in Fig. S5, and no differences regarding the drawn conclusion are observed. Moreover, it is reported that different levels of O_2-saturation could influence the dissolution behavior as well [45], and the Ar-purging allows for the conclusion regarding the balance of plant components as the feed DI water will be O_2-free for large-scale applications.

Before entering the ICP-MS (Agilent 7900, Agilent Technologies), the

downstream electrolyte was mixed with an internal standard solution (^{72}Ge for ^{52}Cr, ^{55}Mn, ^{56}Fe, ^{60}Ni, and ^{95}Mo in 5% HNO_3 (CarlRoth, Ultrapur) prepared from Certipur ICP-MS standard, Merck). The ICP-MS was calibrated daily with standard solutions of all analytes (Certipur ICP-MS standard, Merck). All ICP-MS measurements were performed in the time-resolved analysis mode with a Helium-collision cell ($V_{He} = 4.3$ ml min^{-1}) in low-matrix mode.

All potentials are reported versus the reversible hydrogen electrode (RHE). For measurements in H_2SO_4, the RE potential was measured daily by measuring its open circuit potential in hydrogen-saturated electrolyte versus a Pt-wire (Ø = 0.5 mm, 99.99%, MaTeck). For measurements in DI water, the RE potential was checked daily versus a Master-Ag|AgCl-RE and then shifted according to $E_{RHE} = E_{Ag|AgCl} + E^0_{Ag|AgCl} + 0.059$ pH. No *iR*-correction was applied, a discussion about the estimated influence can be found elsewhere [40].

Two electrochemical protocols were applied. To measure the influence of the potential, the OCP was measured for 300 s followed by potential holds (+100 mV, hold for 90 s) until the final potential of 2 V was reached. The influence of the temperature was measured with the following protocol: Initial hold at 1.2 V for 300 s, three consecutive CV cycles between 1.2 and 2 V with a scan rate of 5 mV s^{-1}, and a final hold at 1.2 V for 300 s. All SFC-ICP-MS measurements were repeated thrice on independent locations, and the different scans are denoted as spot 1–3 per measurement condition in this manuscript.

2.3. Analysis of the dissolution profiles

The data obtained was integrated to determine the dissolved mass. With that value, the dissolved monolayers (ML) were calculated as described elsewhere [40,45]. In short, 316L has a face-centered cubic structure with the lattice parameter a = 0.359 nm [46,47], verified by X-ray diffraction (XRD) measurements (Fig. S1). With that and the average elemental composition of 316L (Table S1 and Table S2), we calculated the amount of metal for 316L and per element that would dissolve for one monolayer of the (111) plane (the most densely packed plane). Dividing this value through the dissolved mass per metal approximates the dissolved ML during the measurement. The dissolution efficiency was calculated for the measurements between 1.2 and 2 V as described elsewhere [40,45]. The following oxidation reactions were assumed based on the Pourbaix-Diagram [48]:

$$2\,Fe + 3\,H_2O \rightarrow Fe_2O_3 + 6\,H^+ + 6\,e^- \quad (1)$$

$$2\,Cr + 3\,H_2O \rightarrow Cr_2O_3 + 6\,H^+ + 6\,e^- \quad (2)$$

$$Ni + H_2O \rightarrow NiO + 2\,H^+ + 2\,e^- \quad (3)$$

$$Mn + 2\,H_2O \rightarrow MnO_2 + 4\,H^+ + 2\,e^- \quad (4)$$

$$Mo + 2\,H_2O \rightarrow MoO_2 + 4\,H^+ + 4\,e^- \quad (5)$$

Moreover, the dissolution profiles were baseline-corrected (subtraction of the lowest measured dissolution rate) before plotting and fitted afterward. The fitted profile was numerically analyzed to determine the peak potentials, onset potentials, and extrema in the dissolution profile. A detailed description of the procedure can be found in the supporting information S3 [40,49].

2.4. SEM and XRD measurements

SEM measurements were performed using a Zeiss Crossbeam 540 FIB-SEM. The accelerating voltage was set to 3 kV with a working distance of 5 mm and a beam current of 750 pA.

XRD was measured in a Rigaku Smartlab SE with a Cu K-α source (8047.8 eV). A divergent beam setup using the cross-beam optics system CBO-α was used, as well as a 1D D/tex Ultra250 detector in reduced X-ray fluorescence mode. The phases of the obtained diffractogram were identified using the software Profex (v. 5.3.0) [50] and the crystallographic structure files PDF #04-007-9753 and PDF #04-002-3692 for α-ferrite and austenite (γ), respectively.

2.5. FIB-lamella and STEM-EDXS

For TEM characterization, thin cross-section lamellae were extracted using the focused ion beam (FIB) lift-out method (Helios Nanolab Dual FIB/SEM, Thermo Fisher, USA). The lamellae were milled down with the Ga^+ beam to a thickness of ~90 nm to achieve electron transparency by gradually lowering the acceleration voltage from 30 kV to 1 kV.

High-angle annular dark field scanning transmission electron microscopy (HAADF-STEM) and energy dispersive X-ray spectroscopy (STEM-EDXS) were performed using a Talos F200i from Thermo Fisher Scientific operated at an acceleration voltage of 200 kV. A probe current of roughly 40 pA and a convergence angle of 10.5 mrad were adjusted.

2.6. EBSD measurements

EBSD measurements were carried out on a Zeiss Gemini 560 equipped with an EDAX Clarity Super EBSD detector (AMETEK Inc., USA). The measurements were executed at 20 kV. After data collection, the EBSD maps were refined via spherical indexing [51] in OIM Matrix (AMETEK) using a pre-calculated master pattern from EMsoft [52].

3. Results and discussion

First, the influence of the potential on the stability of 316L is discussed, followed by the effect of the temperature. To mimic the reported pH conditions in a single cell, two border cases were chosen as electrolytes: DI water, the feed on single cell level, and 0.5 mM H_2SO_4 with a pH of approximately 7 and 3, respectively.

3.1. Influence of the applied potential

As outlined in the introduction, the potential at the anode BPP in PEMWE is currently under discussion. To measure the influence of the potential range on the dissolution stability of 316L, the SFC was approached while measuring the open circuit potential (OCP) in DI water and H_2SO_4 at a stage temperature (T_{stage}) of 60 °C. Then, the potential was increased in 100 mV-steps to a maximum potential of 2 V. In Fig. 1a and b, the stability of 316L in DI water and H_2SO_4 is shown, respectively.

For the DI water case (Fig. 1a), the OCP is at 0.88 ± 0.01 V as soon as the meniscus of the SFC is in contact with the sample (average of 5 s after contact). During the 300 s hold, the OCP fluctuates, but in general, an increase of the OCP is observed for all three measurement spots (average potential during the last 10 s of the OCP hold: 1.07 ± 0.07 V). For Fe, Ni, Mn, and Mo, a peak in the dissolution rate is observed (Table 1) before decreasing again. However, during the fading, smaller peaks or shoulders appear. This is pronounced for the Fe dissolution rate but also observed for Ni and Mn. Most of the time, a slight increase in the measured OCP is detected shortly after the appearance of the shoulders. For Cr, no peak is recognized that deviates significantly from the baseline.

In H_2SO_4 (Fig. 1b), the OCP is around 0.63 ± 0.01 V, gradually decreasing within 69 ± 9 s to 0.38 ± 0.01 V before a sharp drop of the potential to 5 ± 2 mV occurs. During the remaining time of the OCP measurement, the potential increases to 64 ± 2 mV. Immediately after the contact with the sample, dissolution of all elements is detected. Subsequently, almost at the same time as the beginning of the potential drop, a drastic increase in the dissolution rates is observed. The maximum dissolution rates of the elements measured during the initial OCP (Table 1) are notably higher than in DI water. After reaching the maximum, the dissolution rates decrease again but do not reach the baseline within the 300 s OCP measurement. Compared to our previous

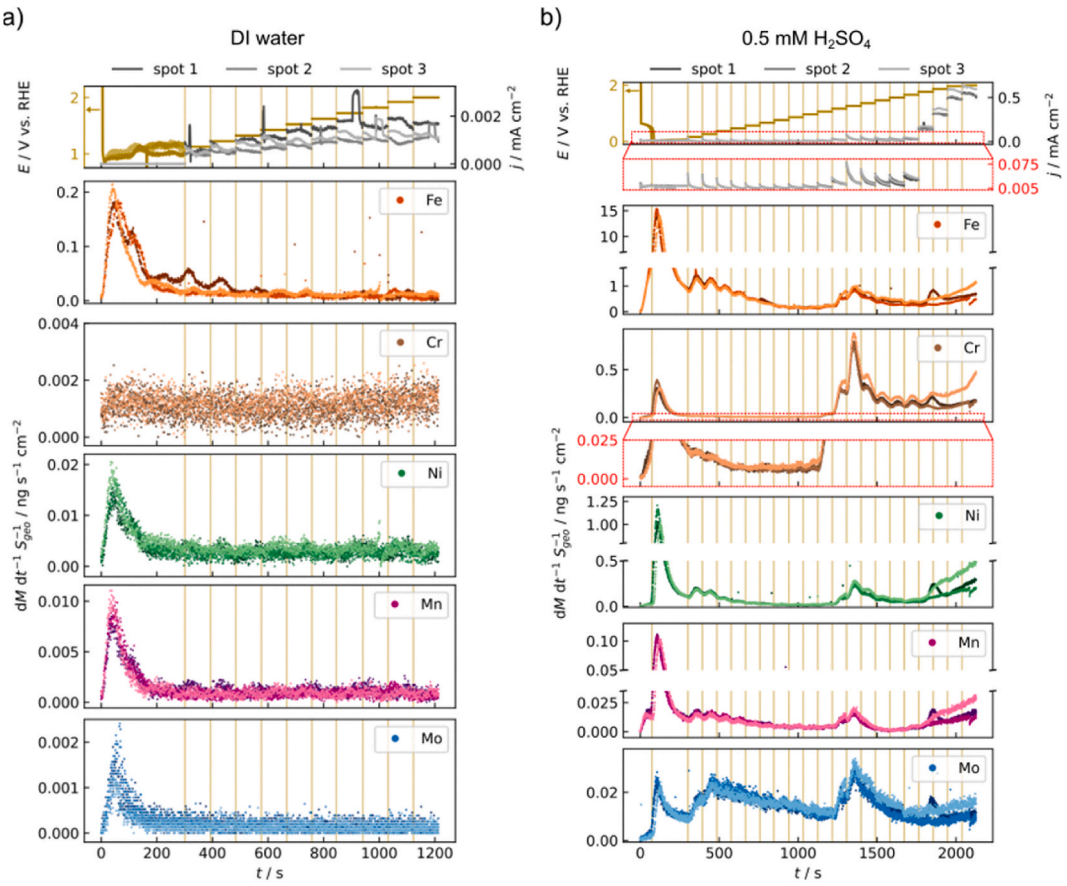

Fig. 1. Dissolution of 316L in a) DI water and b) 0.5 mM H_2SO_4 at T_{stage} = 60 °C. Potential (beige), current density (gray, upper image), and dissolution rates of Fe, Cr, Ni, Mn, and Mo (from top to bottom) for three different spots (dark, medium, and light).

Table 1
Maximum dissolution rate ($dM\ dt^{-1}_{max}$), dissolved metal (m_{OCP}), and respective monolayers (ML_{OCP}) during the 300 s OCP measurement in DI water and 0.5 mM H_2SO_4 at T_{stage} = 60 °C displayed in Fig. 1a and b. In DI water, no values were determined for Cr. The bulk composition of 316L can be found in Table S2.

	Fe	Cr	Ni	Mn	Mo
DI water					
$dM\ dt^{-1}_{max}$/ ng s^{-1} cm^{-2}	0.19 ± 0.02	n.d.[a]	0.067 ± 0.025	0.010 ± 0.001	0.0019 ± 0.0005
m_{OCP}/ng	0.66 ± 0.07	n.d.[a]	0.049 ± 0.008	0.023 ± 0.002	0.0043 ± 0.0013
ML_{OCP}	0.17 ± 0.02	n.d.[a]	0.067 ± 0.011	0.19 ± 0.01	0.028 ± 0.009
H_2SO_4					
$dM\ dt^{-1}_{max}$/ ng s^{-1} cm^{-2}	14.6 ± 0.6	0.34 ± 0.04	1.09 ± 0.03	0.108 ± 0.004	0.026 ± 0.002
m_{OCP}/ng	41.4 ± 1.1	0.96 ± 0.07	3.3 ± 0.3	0.33 ± 0.02	0.10 ± 0.02
ML_{OCP}	10.4 ± 0.3	0.93 ± 0.07	4.5 ± 0.3	2.8 ± 0.2	0.65 ± 0.09

[a] n.d. = not determined.

stability measurements of 316L at the OCP [40], the trends are similar, but the potentials measured for this sample are slightly lower and the dissolution rates are higher. We speculate that this is due to different sample surfaces. For example, Lynch et al. [53] observed different types of oxide layers on 316L, depending on whether the oxide film was native or formed under controlled oxidation conditions. Therefore, we expect different conditions in the laboratory such as temperature or humidity to have an influence.

The dissolved mass per element during the OCP (m_{OCP}) and its estimated equivalent in dissolved monolayers (ML_{OCP}) are displayed in Table 1 (see the experimental section for conversion details, if dissolution would occur as the bulk ratio the amount of calculated dissolved ML would be the same for all elements). In both electrolytes, Fe dissolves preferentially at the OCP. In DI water, the Mn dissolution is also higher than expected from the elemental composition.

During free corrosion at the OCP, 316L serves as anode and cathode with equal anodic and cathodic exchange current densities. Due to the Ar-purging and -blanketing of the electrolyte and hanging meniscus of the SFC, respectively, the reduction of dissolved oxygen in the solution can be excluded as a cathodic reaction. Therefore, the only assumed cathodic reaction on the surface of 316L is the hydrogen evolution reaction (HER) (equation (6)), which is the predominant reaction in acidic media [54]. The anodic reaction would be the metal (Me) dissolution (equation (7)).

$$2\,H^+ + 2\,e^- \rightarrow H_2 \quad (6)$$

$$Me \rightarrow Me^{x+} + x\,e^- \quad (7)$$

We hypothesize that free corrosion occurs during the OCP measurement in DI water and H_2SO_4, leading to changes in the structure of 316L, which explains the OCP-changes and observed dissolution. This process is much more pronounced in H_2SO_4, while in DI water, the native Cr-oxide layer protects the sample from significant dissolution. In H_2SO_4, a protecting Cr-oxide layer will re-form on 316L after initial dissolution of the native oxide layer during the OCP, passivating the surface and, thus, decreasing the dissolution rates. This is supported by the minor Cr dissolution that is much lower than expected from the elemental composition. The preferential dissolution of Fe from 316L at the OCP was already observed in our previous work and by other

researchers, however, partly measured at different conditions [40,53,55]. Lodhi et al. [56] also described a duplex oxide layer structure after 316L exposure to pH 3 in H_2SO_4 with the upper layer being Cr and Fe oxides. Compared to pH 1, a higher amount of Fe but still lower than in the bulk was found [56]. Choudhary et al. [57] also observed a Cr-enrichment at the OCP for 316L, however, no Fe-depletion was observed, which could be explained by NaCl as the used electrolyte as halides are known for enhancing corrosion.

In DI water, the dissolution and current density measured remain very low during the stepwise potential increase from the OCP to 2 V. No further dissolution of Mo is detected. Also, the dissolution rates for Mn and Ni are close to the baseline. The only element with higher detected dissolution rates is Fe. However, the detected dissolution rate increases do not correlate with the stepwise potential increase and appear randomly distributed. During the whole measurement, no significant Cr dissolution is detected. This contrasts the results obtained for the cyclic voltammetry (CV) study in DI water. In our previous work [40] and the temperature study reported below, the predominant dissolution of Cr is observed during CVs between 1.2 and 2 V in DI water. Therefore, we repeated the experiment on a different sample. The results are displayed in Fig. S6. There, similar observations are made – the dissolution of Fe, Ni, Mn, and Mo at the OCP with predominant Fe and Mn dissolution. For the other elements, the dissolution rate decreases to the baseline, while an increase in the Cr dissolution rate can be observed at elevated potentials. Still, the dissolution rate remains very low (below 0.007 ng cm^{-2} s^{-1}). It is also notable that the OCP differs – it is roughly 200 mV higher at the beginning and end of the measurement.

We speculate that the cycling of 316L induces higher Cr dissolution while during the stepwise potential increase, the native Cr-oxide layer on the sample surface protects the 316L better against dissolution and is more stable. For example, faster potential changes experienced by the sample during the CV might influence the behavior. Moreover, the maximum dissolution rate of Cr was observed in the backward scan of the CV. We also think that DI water provides rather mild conditions, and the observed electrochemical and dissolution behavior is much more dominated by the native oxide formed on the sample surface than by the electrolyte. Even though the samples were polished in the same manner one day before measurement, differences in native oxide layer composition, structure, or thickness might possibly explain the slightly different observations, as already mentioned above.

In H_2SO_4, the dissolution behavior is more complex. The dissolved mass per potential step and the corresponding MLs are displayed in Fig. 2. When the potential is increased by +100 mV, the dissolution rates of all elements increase, reaching a maximum dissolution rate that is, however, lower than during the OCP, before decreasing again. Further potential increases also trigger an increase in dissolution. However, the dissolution rate maxima are decreasing, accompanied by a generally decreasing dissolution. Especially for Cr, upon the potential hold at 0.36 V, the dissolution rate only decreases and then remains stable around 0.007 ± 0.001 ng s^{-1} cm^{-2} during the following potential steps. In that time, the dissolution rate of Mo gradually decreases with only minor increases in dissolution rate when the potential is increased. For Fe, Ni, and Mn, the dissolution further decreases and remains almost stable between 0.76 and 0.96 V; however, small dissolution rate peaks are observed for every potential increase. We assume that in this potential range, a stable, protective oxide layer is covering 316L, likely mainly consisting of Cr-oxide. This is also in good agreement with the experimentally constructed E-pH-diagram for 316L by Lothongkum et al. [58] indicating perfect passivation in this potential range as well as indicated by the Pourbaix-Diagram of Cr [48] and corroborated by the small dissolution rates of Cr observed here.

As soon as the potential elevates to 1.06 V in H_2SO_4, the dissolution rates rise again. First, a small increase is observed while for the following potential steps a much higher increase is observed. This effect can be observed especially for Cr, Ni, and Fe. For Cr, the dissolution rate increases to 0.81 ± 0.05 ng s^{-1} cm^{-2}, exceeding the dissolution rate during the OCP, and dissolves above a rate as expected from the elemental composition as the only element. We speculate that at 1.06 V Cr_2O_3 is not stable anymore and is further oxidized to Cr(VI) – the transpassivation begins, which is supported by the Pourbaix-Diagram of Cr [48]. This exposes the underlying metal leading to dissolution of all alloy elements. During these steps also an increase in the current density is observed. Similar onset potentials for the Cr-transpassivation were also reported by other researchers even though measured at different SO_4-electrolyte composition/pH values [59,60].

From 1.36 V, the dissolution rates decrease again and remain relatively similar during the next four potential steps, but on a higher level than during the first stabilization. This indicates a lower passivation of the surface. Such secondary passivation was also observed by other researchers at pH 2 (0.5 M Na_2SO_4 + 0.01 M H_2SO_4) for 316L [59]. From 1.76 V onwards, the current density increases with every potential step reaching 0.57 ± 0.04 mA cm^{-2} at 2 V. This increase in current density is likely caused by the onset of the oxygen evolution reaction (OER). The alloy elements and 316L itself are known OER-catalysts even though mainly used in alkaline media for stability reasons [61–63]. The onset of the OER is accompanied by steadily increasing dissolution rates of all elements. For the measurement on spot 1, an additional peak in the dissolution rate for all elements emerges with its maximum around 1855 s. Shortly before/at the onset of that dissolution event, a spike in the current density signal can be observed for this measurement. We hypothesize that this could relate to a partial detachment of the oxide layer, e.g., through the flow. Three reasons could cause the dissolution by the onsetting OER: First, this potential is high enough that the metals are oxidized [48]. Second, the metals contribute to the OER mechanism

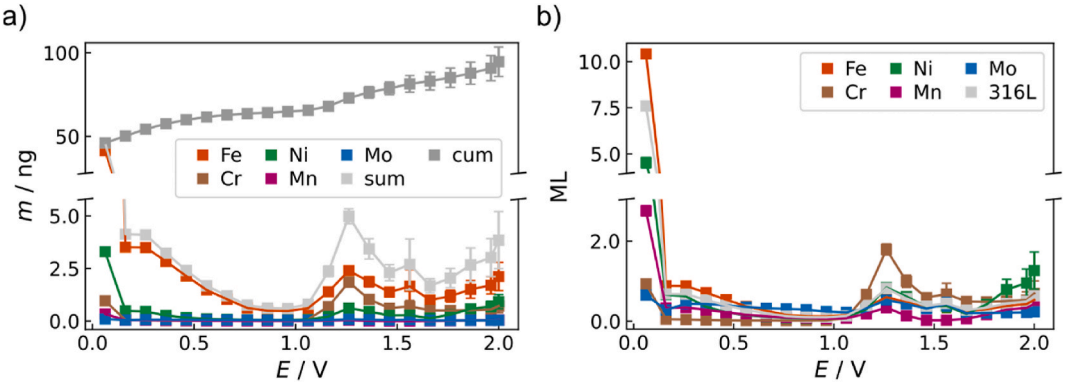

Fig. 2. Dissolution of 316L during each potential hold of the measurement in 0.5 mM H_2SO_4 at T_{stage} = 60 °C displayed in Fig. 1b. a) dissolved mass per element and sum per applied potential step, and cumulative (cum) mass of all elements over the measurement. b) respective ML for every element per applied potential and for 316L if the dissolution would have occurred as expected from the elemental composition.

and dissolve by that as a competitive reaction pathway, as suggested for Ir [64]. Third, the OER causes a local acidification of the surface [65], leading to less dissolution stability of 316L (equation (8)).

$$H_2O \rightarrow 2\,H^+ + 2\,e^- + \frac{1}{2}O_2 \quad (8)$$

The amount of dissolved metal and corresponding MLs over the whole measurement in DI water and H_2SO_4 are listed in Table 2. In both electrolytes, the main fraction already dissolves during the initial OCP – 49% in H_2SO_4 and 72% in DI water. In DI water, the overall dissolution is minor. This is also supported by SEM measurements (Fig. S7): compared to a pristine area no significant corrosion damage is visible. Only in the SEM image with the highest magnification small, slightly darker spots are visible (Fig. S7b). SEM investigations after the electrochemical measurements of one of the spots in H_2SO_4 show signs of corrosion (Fig. 3b and Fig. S7c). This is in good agreement with the high observed dissolution. Corrosion does not occur uniformly on the sample spot, but higher corrosion is observed in some areas of the sample. One possible explanation is that the main fraction dissolved already at the OCP. Here, anodic and cathodic regions are only locally occurring on the sample surface. To investigate the corrosion phenomena in more detail, we prepared a FIB-lift out of one of the corrosion deposits and investigated its nanostructure using STEM-EDXS. The results, as well as a measurement of a pristine area, are shown in Fig. 3.

In the pristine area (Fig. 3a), the homogeneous composition of the sample in the bulk is visible. Near the surface, the oxygen content increases due to the native oxide layer on the surface of the sample (Fig. 3a–v). The thickness of the oxide layer was estimated to be 5.8 ± 3.1 nm (Fig. S8) which is comparable to literature values [55]. In the HAADF-STEM image of the FIB lamella (Fig. 3a–iii), structural changes to a depth of approximately 600 nm are visible. A TEM lamella of the measured sample (Fig. 3b) was lifted out from one of the deposits on the sample surface. Below the deposit, similar structural changes as for the pristine sample are observed (Fig. 3b–iii). No pitting corrosion is observed below the precipitate, however, the surface of the 316L appears rougher. Spectrum images reveal an increasing O-content approximately 500 nm below the sample surface (Fig. 3b–v and Table 3). Fig. 3b–iv - vi reveal the precipitate on the sample surface with a thickness of ~200 nm consists of Fe and O (atomic composition in Table 3).

During the electrochemical measurement, the sample is oxidized, leading to increased oxygen content below the surface. We believe that the species on top of the sample will precipitate during the OCP – there, high Fe dissolution is observed. The atomic ratio suggests a ferrate species ($[FeO_4]^{2-}$). During the OCP, the surface presumably gets more alkaline due to the proton consuming HER (equation (6)), indicating the possible ferrate formation that is known to occur under oxidizing alkaline conditions [66]. A ferric acid was also described as the passive film on Fe in concentrated nitric acid [67]. Moreover, such structural changes are not observed after the CV measurements starting at 1.2 V (Fig. S12).

These results clearly show the importance of testing possible BPP materials at relevant potentials. Our findings indicate that the applied potential on 316L plays a significant role in its dissolution in both DI water and 0.5 mM H_2SO_4 and might affect conclusions drawn to the applicability of 316L or materials in general as BPP. Of course, we like to highlight a possible history effect of the sample by the electrochemical protocol applied that might result in different dissolution behavior if the time per potential step or the potentials themselves are adjusted, for instance, to simulate start stop behavior or the input of fluctuating renewable energies being a study for itself. Nevertheless, the results clearly show the different dissolution regimes of 316L depending on the potential. As already mentioned in the introduction, the "real" potential a BPP experiences on cell level is currently under discussion in the literature, and observed corrosion phenomena of BPPs are in some points rather contradicting [18,20,24–27]. We, therefore, speculate that the performance highly depends on the single cell architecture such as the distance between the anode catalyst layer and BPP (as it is claimed that the corrosive zone drops with distance from the anode catalyst layer [24]), operation mode, quality of water feed, temperatures, and other yet unknown factors. These will influence and change the conditions a BPP experiences *in situ* and might explain the different results described in the introduction on single cell level, as our results show that pH/conductivity and potential have a detrimental influence on observed or non-observed dissolution. Moreover, our results give valuable insights into the stability of uncoated stainless steel in electrolyzers due to coating imperfections of applied coated stainless steel PTLs and/or BPPs and, even more importantly, when stainless steel components are used in the balance of plants as we observe the highest dissolution rates in both electrolytes at the OCP. Contaminations, for example, from water pipes or tanks, have always been a concern for application [37].

3.2. Influence of temperature on dissolution

Temperature influences reaction rates [68]. Thus, to study its effect on the dissolution stability of 316L, the sample was heated to three different T_{stage}, namely 20, 40, and 60 °C, and three consecutive CV cycles between 1.2 and 2 V were recorded before and after a 1.2 V-hold. The measurements were performed in DI water and 0.5 mM H_2SO_4 at randomly chosen locations on the sample (each at three pristine spots per T_{stage}), whose averages with standard deviation per temperature are shown in Fig. 4.

As soon as the SFC is contacted to the sample at 1.2 V during the starting hold, the current density increases in both electrolytes, accompanied by the dissolution of all alloy elements, except Cr in DI water. The maximum current density during the hold increases linearly in DI water and exponentially in H_2SO_4 with higher T_{stage} (Table 4). In DI water, no significant trends of the dissolution rate with T_{stage} are observed (Table S3). In contrast, in H_2SO_4, the maximum dissolution rates during the 1.2 V-hold increase with T_{stage} and are significantly higher (Table S4). The integration of the dissolution profile during the initial 300 s potential hold in H_2SO_4 shows a linear increase of dissolved mass for Fe, Ni, Mn, and Mo, whereas for Cr, it roughly doubles for each 20 °C-increase (Table S5). In both electrolytes, the dissolution rates of the five elements decrease again during the initial hold at 1.2 V. However, in H_2SO_4, the dissolution rate never reaches the baseline again within the 300 s.

When the potential is increased in DI water, predominant dissolution of Cr is observed, independent of T_{stage}. To determine the onsets and the maxima of the observed peaks in the dissolution profile, the single peaks were fitted using a log-normal function, and the onset was defined as 5% of the maximum peak height, as elucidated in the supporting information S3. The obtained values can be found in Table S6–S9 for both electrolytes. The onset potential of Cr dissolution is around 1.7 V for all T_{stage} in DI water (Table S6). The dissolution rates reach their maximum, which is increased with T_{stage} (Table S3), in the backward scan of the CV.

Table 2
Total dissolved mass (m) and corresponding monolayers (ML) of 316L during the whole stepwise potential increase from OCP – 2 V in DI water and 0.5 mM H_2SO_4 at T_{stage} = 60 °C displayed in Fig. 1a and b, respectively.

	Fe	Cr	Ni	Mn	Mo
DI water					
m/ng	0.9 ± 0.3	n.d.	0.08 ± 0.02	0.028 ± 0.003	0.007 ± 0.003
ML	0.23 ± 0.06	n.d.	0.11 ± 0.03	0.23 ± 0.03	0.05 ± 0.02
H_2SO_4					
m/ng	74.3 ± 1.8	8.97 ± 1.50	9.64 ± 0.89	0.78 ± 0.05	1.09 ± 0.06
ML	18.7 ± 1.4	8.7 ± 1.5	13.1 ± 1.3	6.5 ± 0.5	7.2 ± 0.4

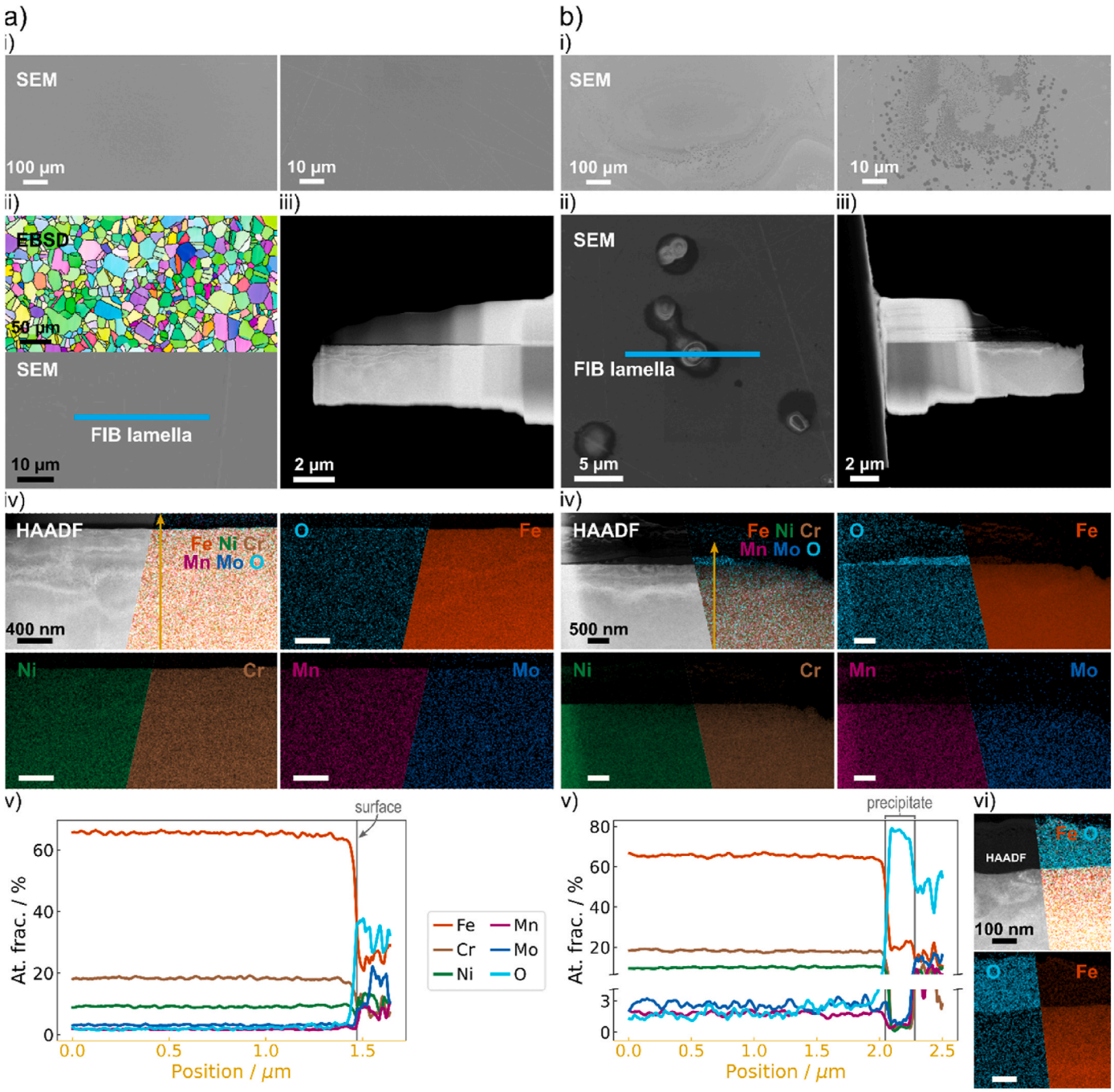

Fig. 3. Microscopic investigation of the pristine sample (a) and after the stepwise potential increase in 0.5 mM H_2SO_4 at T_{stage} = 60 °C (b). a) pristine sample: SEM images and EBSD map (legend refer to Fig. S2) (i and ii), HAADF-STEM image of the FIB-lamella (iii), HAADF-STEM image with corresponding EDX spectrum images (iv), and EDX line profile (v) along the arrow in iv). b) after measurement: SEM images of the sample surface (i and ii) and HAADF-STEM image of the FIB-lamella (iii), HAADF-STEM image with corresponding EDX spectrum images (iv), EDX line profile (v) along the arrow in iv), and zoomed-in HAADF-STEM image with corresponding EDX spectrum images (vi) of the deposit on the cross-section.

Here, the peak potential is reached faster with higher T_{stage} (1.73 ± 0.02 V, 1.63 ± 0.04 V, and 1.57 ± 0.01 V for 60 °C, 40 °C, and 20 °C, respectively; due to the backward scan a higher potential means an earlier maximum). The current density also increases upon potential increase reaching the maximum at the upper vertex potential of the CV (2 V) that increases with higher T_{stage} (Table 4). Also, in the 2nd and 3rd CV cycles, the dissolution behavior is similar, but the current densities and Cr-dissolution rate come closer together, decreasing the differences between the T_{stages}.

Only for the measurement at T_{stage} = 60 °C, slight dissolution of Fe is detected during the three CV scans. However, the positions of the peaks appear rather random and independent of the applied potential as they differ for each of the three measurements (individual measurements shown in Fig. S10). If Fe dissolution is observed, often a very minor peak overlays the Ni dissolution profile. This was not observed in our previous study [40] and measurement on another sample (Fig. S6b). We therefore speculate that this is caused by a slightly different surface as discussed above. Since all measurements of the temperature series in DI water were performed on the same sample and day, the measurements are directly comparable. For Ni, a dissolution profile following the three CV

Table 3
Atomic composition from STEM-EDXS analysis. Bulk composition of the pristine sample and composition of the area with increased O-content below the surface and deposit on the sample surface after measurement in 0.5 mM H_2SO_4 at T_{stage} = 60 °C. The corresponding spectrum image is displayed in Fig. 3a–iv (pristine) and Fig. S9 (after measurement).

	Fe/at%	Cr/at%	Ni/at%	Mn/at%	Mo/at %	O/at%
Bulk	66.9 ± 3.5	17.1 ± 2.5	9.6 ± 1.6	1.2 ± 0.3	4.7 ± 1.6	0.5 ± 0.1
Oxide layer	64.5 ± 3.6	17.1 ± 2.4	10.1 ± 1.6	1.2 ± 0.3	2.4 ± 0.4	4.8 ± 0.5
Deposit	14.9 ± 1.7	0.32 ± 0.05	0.14 ± 0.03	0.14 ± 0.03	0.8 ± 0.2	83.7 ± 1.7

cycles is observed (Table S3).

In 0.5 mM H_2SO_4, the electrochemical and dissolution behavior of 316L is notably higher. Upon potential increase, the dissolution rates of all elements except Mn increase with decreasing onset potential with higher T_{stage} (Table S8). For all elements, the dissolution sets in the latest around 1.32 V, 1.42 V, and 1.47 V at T_{stage} = 60 C, 40 °C, and 20 °C, respectively. For Cr and Ni, the dissolution rate peaks, while for Fe and Mo, the dissolution rate stabilizes, forming a shoulder to the 2nd observed peak. The Cr dissolution rates reach the maximum first and Cr is the only element showing a trend for the peak potential with T_{stage} – it decreases with T_{stage} (Table S9). Like the dissolution rate, the current density increases with increased potential. First, the current density is the highest at T_{stage} = 60 °C, but at approximately 1.36 V, the current densities intersect and the one at 20 °C is the highest, followed by the one at 40 °C and 60 °C. For the measurements at 40 °C and 60 °C, the current density reaches a plateau at ~1.55 V and ~1.5 V at 0.027 ± 0.001 mA cm^{-2} and 0.025 ± 0.001 mA cm^{-2}, respectively, whereas for the measurement at 20 °C, a peak in current density (0.031 ± 0.001 mA cm^{-2} at ~1.5 V) is observed. The current increases sharply between 1.6 and 1.7 V (the higher T_{stage}, the earlier the increase), ascribed to the onset of the OER. The onset of the 2nd peak in the 1st cycle of the dissolution rate is determined by the fitting procedure shortly after that current increase (Table S8). For Fe, Cr, and Ni, a higher T_{stage} leads to a later onset, whereas for Mn and Mo, no trend is observed. We speculate that different thicknesses of the oxide formed could cause this.

The maximum current density reached at the upper potential limit of the CV scan (2 V) is similar for 60 °C and 40 °C, whereas it is lower for the measurement at 20 °C (Table 4). The maximum dissolution rates of the 2nd peak are reached in the backward scan for all elements. Especially for Cr, the peak potential increases with T_{stage} (a higher potential means an earlier reached maximum in the backward CV scan). Moreover, the ratio of the 1st and 2nd peak of Cr in the 1st CV cycle highly depends on T_{stage}. At 20 °C, the maximum dissolution rate is halved for the 2nd peak. For 40 °C, the heights are the same (in the range of error), whereas for 60 °C, a minor increase for the 2nd peak is observed (Table S4). We think the first dissolution peak is caused by oxidation and a slightly re-passivating surface. According to the stepwise potential increase (Fig. 1b), the contacting of the SFC occurs in the transpassivation range accelerated by T_{stage}. The scanning results in further dissolution due to oxidation accompanied by secondary passivation of the surface, which is proven by decreasing/stabilizing dissolution rates and current densities. This secondary passivation is initially reached faster with a higher T_{stage}. We speculate that the OER mainly causes the 2nd dissolution peak. This is indicated by the close measured dissolution

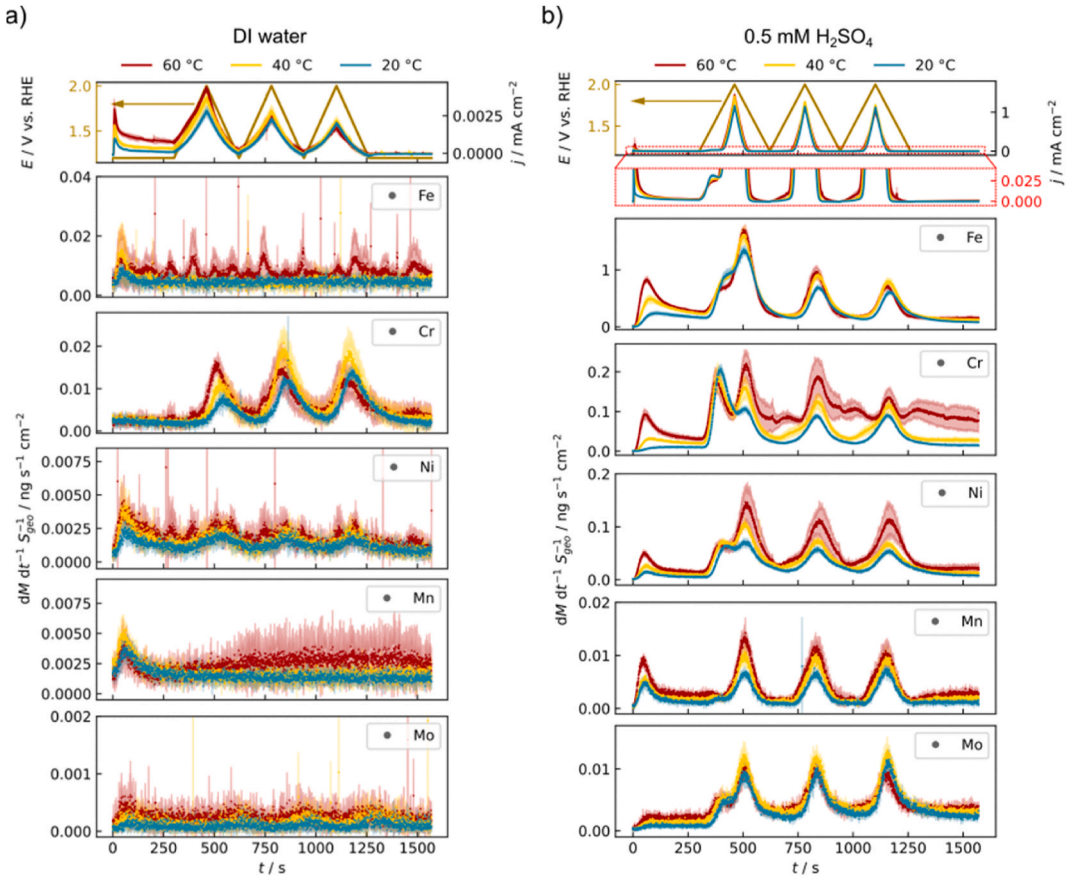

Fig. 4. Temperature-dependent dissolution of 316L in a) DI water and b) 0.5 mM H_2SO_4. Potential profile (beige) and current density (upper image) and dissolution rates of Fe, Cr, Ni, Mn, and Mo (from top to bottom) at three different T_{stage} (20 °C - blue, 40 °C – yellow, and 60 °C - red) – average of three measurements per T_{stage} on different spots with standard deviation.

Table 4
Current densities during contact and at 2 V vs. RHE per cycle, transferred charge during the whole measurement, and dissolution efficiency in DI water and 0.5 mM H_2SO_4 for three different T_{stage}.

T_{stage}/ °C	Contact/ mA cm^{-2}	1st cycle/ mA cm^{-2}	2nd cycle/ mA cm^{-2}	3rd cycle/ mA cm^{-2}	Transferred charge/mC	Dissolution efficiency/ %
DI water						
20	(1.01 ± 0.05) 10^{-3}	(2.90 ± 0.21) 10^{-3}	(2.37 ± 0.09) 10^{-3}	(2.07 ± 0.05) 10^{-3}	(32.8 ± 0.9) 10^{-3}	3.50 ± 0.24
40	(2.00 ± 0.11) 10^{-3}	(3.81 ± 0.39) 10^{-3}	(2.88 ± 0.32) 10^{-3}	(2.00 ± 0.11) 10^{-3}	(45.5 ± 5.9) 10^{-3}	4.49 ± 0.39
60	(3.08 ± 0.29) 10^{-3}	(4.42 ± 0.07) 10^{-3}	(2.53 ± 0.30) 10^{-3}	(1.84 ± 0.14) 10^{-3}	(54.3 ± 2.9) 10^{-3}	5.20 ± 1.01
H_2SO_4						
20	0.05 ± 0.02	1.17 ± 0.01	1.14 ± 0.03	1.12 ± 0.03	5.8 ± 0.1	2.00 ± 0.04
40	0.11 ± 0.02	1.40 ± 0.01	1.26 ± 0.02	1.18 ± 0.03	7.1 ± 0.1	2.08 ± 0.08
60	0.29 ± 0.05	1.43 ± 0.05	1.20 ± 0.04	1.03 ± 0.05	7.5 ± 0.3	2.16 ± 0.15

rates and current densities at T_{stage} = 40 and 60 °C while being significantly lower at T_{stage} = 20 °C. Temperature is a known factor to enhance the activity of OER catalysts [69]. The higher dissolution might be due to a higher turnover frequency of the active centers that increase the chance of concurring reactions such as dissolution or a slightly higher acidification due to the higher H^+ formation.

In the 2nd and 3rd CV scans, a trend of decreasing dissolution is observed (Fig. 4b and Table S4). There, only one peak is observed for every element except Cr. For Cr, the situation is more complicated. For the measurement at T_{stage} = 20 and 40 °C, only one peak is observed, whereas for the measurement at 60 °C, multiple increases in the dissolution rate are observed. However, the position of these increases is not the same (Fig. S11), leading to a rather high standard deviation. In the following, only the onset and maximum of the main dissolution peak occurring at the same time as the dissolution of the other elements is regarded. We speculate that this behavior comes from the protecting Cr-oxide layer formed on 316L whose stability might be lower at higher temperatures. One reason could be that the passive film is less-ordered with more defects that are prone to more sudden dissolution events. The microstructure itself with preferential dissolution from grain boundaries or specific planes can be likely excluded as EBSD mappings prove a very high number of grains per SFC spot averaging that influence out (Fig. 3a–ii and section S1.2. in the supporting information). The peak maximum appears to be rather independent of T_{stage} for Cr, Ni, Mn, and Mo. Only for Fe, a very small shift of the peak maximum to lower potentials can be observed with decreasing T_{stage} (Table S8). As in DI water, the current densities are decreasing with cycling, especially for 60 °C and 40 °C (Table 4). This speaks as well for continuing passivation and deactivation of the sample at all three T_{stage}.

In both electrolytes, the total dissolved mass and corresponding MLs over the whole measurement time are enhanced with T_{stage} (Fig. 5, refer to Table S9 for exact values). The enhanced corrosion with higher T_{stage} was also reported for 316L and 304 in a mimicked fuel cell environment (diluted H_2SO_4 with F^-) [70,71]. It is clearly visible that the dissolution in DI water is in sum two orders of magnitude lower compared to 0.5 mM H_2SO_4.

In DI water, Cr dissolution increases from T_{stage} = 20 to 40 °C by ~50%, whereas no further increase is observed from 40 °C to 60 °C. The calculated MLs also reveal the predominant dissolution of Cr and Mn. For Mn, a high increase in dissolution is observed from 40 °C to 60 °C. However, this is mainly caused by one measurement with an increased dissolution rate (spot 1 in Fig. S10). For the two other measurements (spots 2 and 3), the integration of the dissolution profile of Mn also results in a higher dissolution at 40 °C but the impact is remarkably less. We speculate that a defect in the oxide layer causes this. Altogether, the dissolution of 316L is very low, and in total, not even one ML of 316L dissolves during the measurement, as previously shown at a stage temperature of 60 °C [40].

We speculate that during the initial hold, 316L slightly dissolves. However, Cr remains stable and forms an oxide layer. Combined with

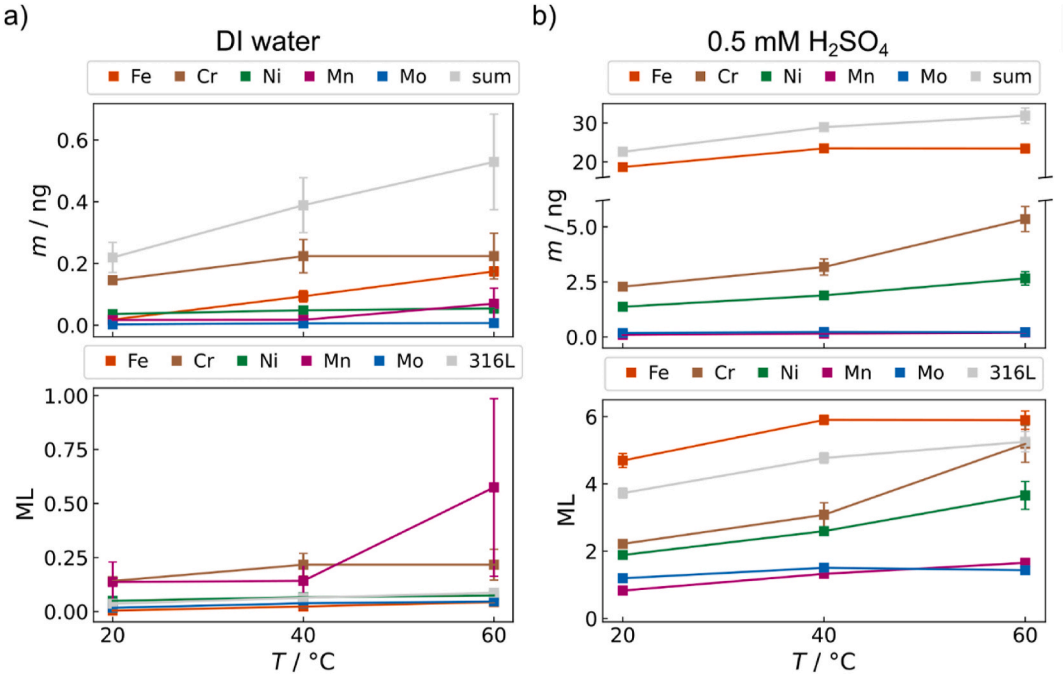

Fig. 5. Total amount of dissolved metal and corresponding monolayers (ML) in dependence of T_{stage} during the SFC-ICP-MS measurements of 316L in a) DI water and b) 0.5 mM H_2SO_4 displayed in Fig. 4.

the native Cr-enriched oxide layer on top of the 316L the sample is very dissolution-stable in DI water. With cycling, only the top layer (Cr) dissolves at a very low rate, so the underlying bare 316L is not exposed and remains protected at every measured temperature.

In H_2SO_4, the dissolved mass increases by ~30% from 20 °C to 40 °C and by another ~10% for the increase to 60 °C. However, looking at the elements themselves, the trend differs for each element. For Fe, the amount of dissolved metal increases by 26% upon the temperature increase from 20 °C to 40 °C, but remains similar for the increase from 40 °C to 60 °C. Similar observations are made for Mo. For Ni, the dissolution increases by ~40% per T_{stage} increase while Mn increases linearly. For Cr, the dissolution increases by ~40% and ~70% for each 20 °C-increase. For all three T_{stage}, the dissolution of Fe is higher than expected from the composition of 316L (20 °C: 83 wt%, 40 °C: 81 wt%, 60 °C: 74 wt%). However, the increase from 40 °C to 60 °C changes the dissolution behavior of 316L – Cr now dissolves at a level as expected from the elemental composition. This change follows previous reports of a lower relative Cr-content while the relative Fe-content in passive films increased for 316L and 304 with increased T [70,71]. Combined with the much higher Cr-dissolution rate, also during the final 1.2 V hold, at T_{stage} = 60 °C compared to the other temperatures and observed spontaneous increase in dissolution rate, this speaks for a lowered Cr stability at higher temperatures in H_2SO_4. Compared to our previous study, only at T_{stage} = 60 °C, the shape of the dissolution curve and the dissolution behavior of the sample are very similar [40]. Again, as already for the measurement starting at the OCP, slight differences in the native oxide layer of the 316L might explain the different dissolution rates.

Moreover, the current was integrated to determine the transferred charge and estimate the dissolution efficiency (DE). The electrochemical activity of the sample is highly decreased in DI water compared to H_2SO_4 but the trends are the same – in both electrolytes, the transferred charge slightly increases with increased T_{stage} but the DEs are rather similar (Table 4). In both electrolytes, the DE is low indicating that most of the current is consumed for processes other than dissolution. Especially in H_2SO_4, we assume the main current sink being the OER at elevated potentials and another, minor part the oxide layer formation on the surface.

After the SFC-ICP-MS measurements, SEM characterizations of the samples were conducted, as displayed in Fig. 6 (further images in Fig. S12 and Fig. S13). After measurement in DI water, no significant signs of corrosion are visible, consistent with the very low dissolution. However, scratches are visible in some parts of the sample with the in-lens-detector, which were also visible in some parts of the pristine sample. These surface inhomogeneities might explain the random Fe dissolution events as this was not observed for another sample (Fig. 3b) and our previous study [40]. After measurement in H_2SO_4, clear signs of corrosion are visible for all T_{stage}. The number of macroscopic defects increases with increased T_{stage} (SEM image with lowest magnification). However, at high magnification, signs of corrosion (darker regions in the µm-range) are visible at T_{stage} = 20 °C. With higher T_{stage}, the corrosion signs are slightly enhanced and the whole sample seems rougher. These observations align well with the results from the SFC-ICP-MS measurements. Differences in dissolution are obvious but remain in the same order of magnitude. Therefore, only such slight differences are expected between the different T_{stage} while the difference to the measurements in DI water is visible.

Our results show the influence of the temperature on the dissolution stability of 316L. An increase in dissolution is observable at both tested pH values, 3 and 7. In DI water, even at T_{stage} = 60 °C, the dissolution remains at a very low level, showing the high dissolution stability of 316L at these conditions due to the low conductivity and near neutral pH value. The temperature influences the dissolution behavior at a lower pH value and higher conductivity (0.5 mM H_2SO_4). Even though the dissolution of the elements is in the same order of magnitude, it is enhanced by the temperature, and especially the Cr dissolution rate is enhanced, which might lead to a less stable passivation of the sample as the Cr-oxide layer on top of 316L is known for its protecting abilities [55].

4. Conclusion

In this study, we investigated the influence of the applied potential and the temperature on the dissolution of stainless steel 316L in two electrolytes (DI water with a pH ≈ 7, and 0.5 mM H_2SO_4 with a pH ≈ 3). We showed that in DI water the dissolution of 316L is very low. At the OCP and following stepwise potential increase to 2 V, predominant Fe and Mn dissolution is observed, while during cycling (between 1.2 and 2 V) Cr dissolution dominates. However, the impact of DI water on the sample is low, and the electrochemical and dissolution behavior could be mainly influenced by the native oxide layer on the sample, which protects it well against dissolution. In 0.5 mM H_2SO_4, the applied potential plays a significant role in the dissolution behavior – at the OCP, predominant and high Fe dissolution is observed. However, 316L is protected against significant dissolution afterward until Cr-transpassivation sets in. Secondary passivation is observed, but the OER triggers further dissolution. During CV measurements (1.2–2 V), dissolution of all alloy elements is observed at all tested temperatures (20, 40, and 60 °C). Fe dissolves predominantly at all stage

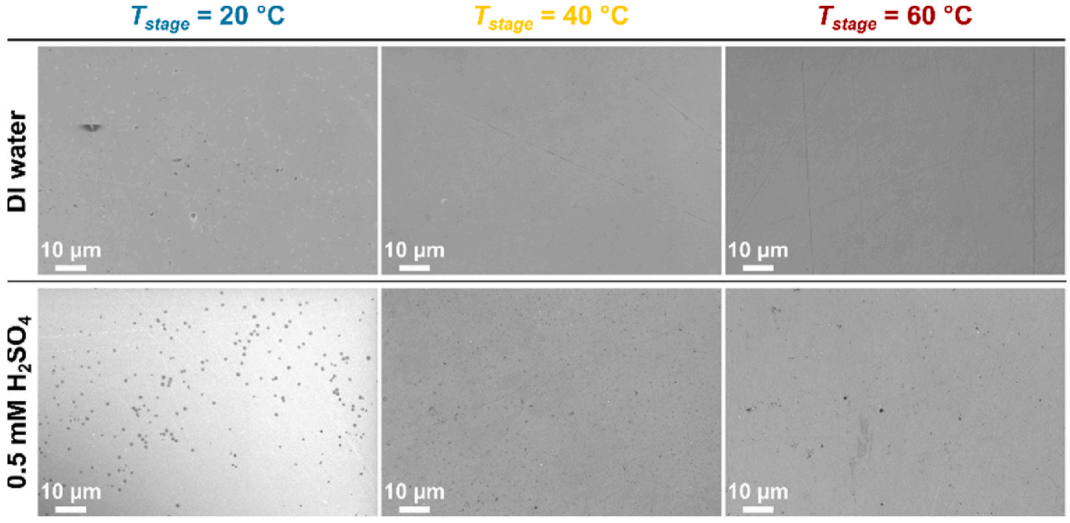

Fig. 6. SEM images of 316L after measurement in DI water and 0.5 mM H_2SO_4 are shown in Fig. 4. Further SEM images can be found in Fig. S12 and S13.

temperatures, however, from 40 °C to 60 °C the dissolution stability of Cr significantly decreases indicating a lower stability of the protective Cr oxide layer. Compared to DI water, the dissolution is notably enhanced in 0.5 mM H_2SO_4.

Both results clearly emphasize the importance of *ex situ* testing conditions for possible BPP materials for PEMWE. Especially in acidic media, the dissolution behavior of 316L highly depends on the applied potential and protocol. Mimicking the conditions the BPP experiences in an operating single cell is important to draw meaningful conclusions. If a potential below the Cr-transpassivation is chosen, stability of 316L might be assumed – however, if the potential in an operating single cell is higher or lower this could lead to unexpected dissolution that might harm the system. However, the "real" conditions of a BPP are under discussion, and more investigation of the potential, pH values, and conductivity of the water feed is needed.

Currently, *ex situ* testing should be performed in various pH ranges and potential windows to get a better idea of the possibilities but also limitations of the used materials while mimicking operational conditions. The results show that 316L requires coatings if used as BPP material in PEMWE for two reasons – first, to protect the BPP from dissolution and second to improve the ICR, a factor that requires more attention in future studies. Moreover, they give insights about possible contaminations whenever unprotected steel exists in PEM electrolyzers, either in the balance of plant or due to coating imperfections.

CRediT authorship contribution statement

Lena Fiedler: Writing – original draft, Visualization, Investigation, Formal analysis, Conceptualization. **Tien-Ching Ma:** Writing – review & editing, Investigation. **Birk Fritsch:** Writing – review & editing, Visualization, Formal analysis. **Martin Dierner:** Writing – review & editing, Investigation. **Darius Hoffmeister:** Writing – review & editing, Investigation, Formal analysis. **Carmen Rubach:** Writing – review & editing, Investigation. **Johannes Will:** Writing – review & editing, Supervision. **Thomas Przybilla:** Writing – review & editing, Supervision. **Erdmann Spiecker:** Writing – review & editing, Supervision, Resources. **Dominik Dworschak:** Writing – review & editing, Resources, Data curation. **Karl J.J. Mayrhofer:** Writing – review & editing, Supervision, Resources, Funding acquisition, Conceptualization. **Andreas Hutzler:** Writing – review & editing, Visualization, Supervision, Resources, Project administration, Investigation, Conceptualization.

Data and code availability

Upon reasonable request, the data that support the findings of this study are available from the corresponding authors.

The code used for the fitting of the dissolution profiles is available on GitHub: https://github.com/BirkFritsch/SFC-ICPMS-Fitting.

Declaration of competing interest

The authors declare that they have no known competing financial interests or personal relationships that could have appeared to influence the work reported in this paper.

Acknowledgments

We thank Nico Röttcher for his help and maintenance of a SQL- and Python-based data evaluation and visualization and Maximilian Maier for supporting AFM measurements.

Lena Fiedler, Tien-Ching Ma, Darius Hoffmeister, and Andreas Hutzler gratefully acknowledge the financial support by the German Federal Ministry of Education and Research (BMBF) via the project StacIE (FKZ: 03HY103H) and Dominik Dworschak via the project HyThroughGen (FKZ: 03HY108A) both within the H_2Giga flagship project.

Appendix A. Supplementary data

Supplementary data to this article can be found online at https://doi.org/10.1016/j.mtsust.2025.101155.

Data availability

Data will be made available on request.

References

[1] A.M. Oliveira, R.R. Beswick, Y. Yan, A green hydrogen economy for a renewable energy society, Curr. Opin. Chem. Eng. 33 (2021), https://doi.org/10.1016/j.coche.2021.100701.
[2] Bundesministerium für Wirtschaft und Klimaschutz (BMWK) (Hrsg.), Fortschreibung der Nationalen Wasserstoffstrategie, Berlin, 2023.
[3] IEA, Global Hydrogen Review 2024, IEA, Paris, 2024.
[4] IRENA, Making the breakthrough - green hydrogen policies and technology costs, International Renewable Energy Agency (2021). Abu Dhabi.
[5] M. Carmo, D.L. Fritz, J. Mergel, D. Stolten, A comprehensive review on PEM water electrolysis, Int. J. Hydrogen Energy 38 (2013) 4901–4934, https://doi.org/10.1016/j.ijhydene.2013.01.151.
[6] M. Chatenet, B.G. Pollet, D.R. Dekel, F. Dionigi, J. Deseure, P. Millet, R.D. Braatz, M.Z. Bazant, M. Eikerling, I. Staffell, P. Balcombe, Y. Shao-Horn, H. Schafer, Water electrolysis: from textbook knowledge to the latest scientific strategies and industrial developments, Chem. Soc. Rev. 51 (2022) 4583–4762, https://doi.org/10.1039/d0cs01079k.
[7] C. Wang, K. Lee, C.P. Liu, D. Kulkarni, P. Atanassov, X. Peng, I.V. Zenyuk, Design of PEM water electrolysers with low iridium loading, Int. Mater. Rev. 69 (2024) 3–18, https://doi.org/10.1177/09506608231216665.
[8] B. Tamilarasi, K.P. Jithul, J. Pandey, Non-noble metal-based electro-catalyst for the oxygen evolution reaction (OER): towards an active & stable electro-catalyst for PEM water electrolysis, Int. J. Hydrogen Energy 58 (2024) 556–582, https://doi.org/10.1016/j.ijhydene.2024.01.222.
[9] D. Hoffmeister, S. Finger, L. Fiedler, T.C. Ma, A. Korner, M. Zlatar, B. Fritsch, K. W. Bodnar, S. Carl, A. Gotz, B.A. Zubiri, J. Will, E. Spiecker, S. Cherevko, A.T. S. Freiberg, K.J.J. Mayrhofer, S. Thiele, A. Hutzler, C. van Pham, Photodeposition-based synthesis of TiO_2@IrO_x core-shell catalyst for proton exchange membrane water electrolysis with low iridium loading, Adv. Sci. 11 (2024) e2402991, https://doi.org/10.1002/advs.202402991.
[10] D. Hoffmeister, S. Finger, R. Pokhrel, A. Körner, B. Fritsch, S. Thiele, A. Hutzler, C. Pham, Structural optimization of TiO_2@IrO_2 catalyst for proton exchange membrane water electrolysis, Chem. Eng. 517 (2025), https://doi.org/10.1016/j.cej.2025.164281.
[11] T.-C. Ma, A. Hutzler, B. Bensmann, R. Hanke-Rauschenbach, S. Thiele, Influence of the complex interface between transport and catalyst layer on water electrolysis performance, J. Electrochem. Soc. 171 (2024), https://doi.org/10.1149/1945-7111/ad3497.
[12] IRENA, Green Hydrogen Cost Reduction: Scaling up Electrolysers to Meet the 1.5°C Climate Goal, 2020. Abu Dhabi.
[13] H. Teuku, I. Alshami, J. Goh, M.S. Masdar, K.S. Loh, Review on bipolar plates for low-temperature polymer electrolyte membrane water electrolyzer, Int. J. Energy Res. 45 (2021) 20583–20600, https://doi.org/10.1002/er.7182.
[14] K.W. Ahmed, M.J. Jang, M.G. Park, Z. Chen, M. Fowler, Effect of components and operating conditions on the performance of PEM electrolyzers: a review, Electrochem 3 (2022) 581–612, https://doi.org/10.3390/electrochem3040040.
[15] S. Mahabunphachai, Ö.N. Cora, M. Koç, Effect of manufacturing processes on formability and surface topography of proton exchange membrane fuel cell metallic bipolar plates, J. Power Sources 195 (2010) 5269–5277, https://doi.org/10.1016/j.jpowsour.2010.03.018.
[16] S. Lædre, O.E. Kongstein, A. Oedegaard, H. Karoliussen, F. Seland, Materials for Proton Exchange Membrane water electrolyzer bipolar plates, Int. J. Hydrogen Energy 42 (2017) 2713–2723, https://doi.org/10.1016/j.ijhydene.2016.11.106.
[17] A. Kellenberger, N. Vaszilcsin, D. Duca, M.L. Dan, N. Duteanu, S. Stiber, T. Morawietz, I. Biswas, S.A. Ansar, P. Gazdzicki, F.J. Wirkert, J. Roth, U. Rost, M. Brodmann, A.S. Gago, K.A. Friedrich, Towards replacing titanium with copper in the bipolar plates for proton exchange membrane water electrolysis, Materials 15 (2022), https://doi.org/10.3390/ma15051628.
[18] L. Messing, K. Pellumbi, L. Hoof, N. Imming, S. Wilbers, L. Kopietz, M. Joemann, A. Grevé, K. junge Puring, U.P. Apfel, Carbon bipolar plates in PEM water electrolysis: bust or must? Adv. Energy Mater. (2024) 2402308 https://doi.org/10.1002/aenm.202402308.
[19] M. Langemann, D.L. Fritz, M. Müller, D. Stolten, Validation and characterization of suitable materials for bipolar plates in PEM water electrolysis, Int. J. Hydrogen Energy 40 (2015) 11385–11391, https://doi.org/10.1016/j.ijhydene.2015.04.155.
[20] H. Becker, L. Castanheira, G. Hinds, Local measurement of current collector potential in a polymer electrolyte membrane water electrolyser, J. Power Sources 448 (2020) 227563, https://doi.org/10.1016/j.jpowsour.2019.227563.
[21] A.S. Gago, S.A. Ansar, B. Saruhan, U. Schulz, P. Lettenmeier, N.A. Cañas, P. Gazdzicki, T. Morawietz, R. Hiesgen, J. Arnold, K.A. Friedrich, Protective coatings on stainless steel bipolar plates for proton exchange membrane (PEM) electrolysers, J. Power Sources 307 (2016) 815–825, https://doi.org/10.1016/j.jpowsour.2015.12.071.

[22] N. Rojas, M. Sánchez-Molina, G. Sevilla, E. Amores, E. Almandoz, J. Esparza, M. R. Cruz Vivas, C. Colominas, Coated stainless steels evaluation for bipolar plates in PEM water electrolysis conditions, Int. J. Hydrogen Energy 46 (2021) 25929–25943, https://doi.org/10.1016/j.ijhydene.2021.03.100.
[23] M. Prestat, Corrosion of structural components of proton exchange membrane water electrolyzer anodes: a review, J. Power Sources 556 (2023) 232469, https://doi.org/10.1016/j.jpowsour.2022.232469.
[24] H. Becker, E.J.F. Dickinson, X. Lu, U. Bexell, S. Proch, C. Moffatt, M. Stenström, G. Smith, G. Hinds, Assessing potential profiles in water electrolysers to minimise titanium use, Energy Environ. Sci. 15 (2022) 2508–2518, https://doi.org/10.1039/d2ee00876a.
[25] L.H. Prado, S. Virtanen, N. Weineck, A. Ghicov, F. Kessler, How to perform corrosion experiments for proton exchange membrane water electrolysis bipolar plates, J. Power Sources 613 (2024), https://doi.org/10.1016/j.jpowsour.2024.234815.
[26] H.-Y. Jung, S.-Y. Huang, P. Ganesan, B.N. Popov, Performance of gold-coated titanium bipolar plates in unitized regenerative fuel cell operation, J. Power Sources 194 (2009) 972–975, https://doi.org/10.1016/j.jpowsour.2009.06.030.
[27] K.U. Hansen, A. Lee, F. Jiao, Enabling low-IrO2 proton exchange membrane water electrolysis via microporous layer-supported catalyst-coated membranes, Chem Catal. 4 (2024) 101036, https://doi.org/10.1016/j.checat.2024.101036.
[28] S. Wu, W. Yang, H. Yan, X. Zuo, Z. Cao, H. Li, M. Shi, H. Chen, A review of modified metal bipolar plates for proton exchange membrane fuel cells, Int. J. Hydrogen Energy 46 (2021) 8672–8701, https://doi.org/10.1016/j.ijhydene.2020.12.074.
[29] K. Karacan, S. Celik, S. Toros, M. Alkan, U. Aydin, Investigation of formability of metallic bipolar plates via stamping for light-weight PEM fuel cells, Int. J. Hydrogen Energy 45 (2020) 35149–35161, https://doi.org/10.1016/j.ijhydene.2020.01.251.
[30] S. Porstmann, T. Wannemacher, W.G. Drossel, A comprehensive comparison of state-of-the-art manufacturing methods for fuel cell bipolar plates including anticipated future industry trends, J. Manuf. Process. 60 (2020) 366–383, https://doi.org/10.1016/j.jmapro.2020.10.041.
[31] P. Lettenmeier, R. Wang, R. Abouatallah, F. Burggraf, A.S. Gago, K.A. Friedrich, Coated stainless steel bipolar plates for proton exchange membrane electrolyzers, J. Electrochem. Soc. 163 (2016) F3119–F3124, https://doi.org/10.1149/2.0141611jes.
[32] S. Stiber, N. Sata, T. Morawietz, S.A. Ansar, T. Jahnke, J.K. Lee, A. Bazylak, A. Fallisch, A.S. Gago, K.A. Friedrich, A high-performance, durable and low-cost proton exchange membrane electrolyser with stainless steel components, Energy Environ. Sci. 15 (2022) 109–122, https://doi.org/10.1039/d1ee02112e.
[33] S. Stiber, M. Hehemann, M. Carmo, M. Müller, K.E. Ayers, C. Capuano, N. Danilovic, T. Morawietz, I. Biswas, P. Gazdzicki, J.F. Heger, A.S. Gago, K. A. Friedrich, Long-term operation of Nb-coated stainless steel bipolar plates for proton exchange membrane water electrolyzers, Adv. Energy Sustain. Res. 3 (2022) 2200024, https://doi.org/10.1002/aesr.202200024.
[34] P. Lettenmeier, R. Wang, R. Abouatallah, B. Saruhan, O. Freitag, P. Gazdzicki, T. Morawietz, R. Hiesgen, A.S. Gago, K.A. Friedrich, Low-cost and durable bipolar plates for proton exchange membrane electrolyzers, Sci. Rep. 7 (2017) 44035, https://doi.org/10.1038/srep44035.
[35] A.S. Gago, A.S. Ansar, P. Gazdzicki, N. Wagner, J. Arnold, K.A. Friedrich, Low cost bipolar plates for large scale PEM electrolyzers, ECS Trans. 64 (2014) 1039–1048, https://doi.org/10.1149/06403.1039ecst.
[36] N. Li, S.S. Araya, S.K. Kær, The effect of Fe3+ contamination in feed water on proton exchange membrane electrolyzer performance, Int. J. Hydrogen Energy 44 (2019) 12952–12957, https://doi.org/10.1016/j.ijhydene.2019.04.015.
[37] H. Becker, J. Murawski, D.V. Shinde, I.E.L. Stephens, G. Hinds, G. Smith, Impact of impurities on water electrolysis: a review, Sustain. Energy Fuels 7 (2023) 1565–1603, https://doi.org/10.1039/d2se01517j.
[38] H. Wang, J.A. Turner, The influence of metal ions on the conductivity of Nafion 112 in polymer electrolyte membrane fuel cell, J. Power Sources 183 (2008) 576–580, https://doi.org/10.1016/j.jpowsour.2008.05.077.
[39] M.J. Kelly, G. Fafilek, J.O. Besenhard, H. Kronberger, G.E. Nauer, Contaminant absorption and conductivity in polymer electrolyte membranes, J. Power Sources 145 (2005) 249–252, https://doi.org/10.1016/j.jpowsour.2005.01.064.
[40] L. Fiedler, T.C. Ma, B. Fritsch, J.H. Risse, M. Lechner, D. Dworschak, M. Merklein, K.J.J. Mayrhofer, A. Hutzler, Stability of bipolar plate materials for proton-exchange membrane water electrolyzers: dissolution of titanium and stainless steel in DI water and highly diluted acid, ChemElectroChem 10 (2023) e202300373, https://doi.org/10.1002/celc.202300373.
[41] O. Kasian, S. Geiger, K.J.J. Mayrhofer, S. Cherevko, Electrochemical on-line ICP-MS in electrocatalysis research, Chem. Rec. 19 (2019) 2130–2142, https://doi.org/10.1002/tcr.201800162.
[42] S.O. Klemm, A.A. Topalov, C.A. Laska, K.J.J. Mayrhofer, Coupling of a high throughput microelectrochemical cell with online multielemental trace analysis by ICP-MS, Electrochem. Commun. 13 (2011) 1533–1535, https://doi.org/10.1016/j.elecom.2011.10.017.
[43] K. Ogle, Atomic emission spectroelectrochemistry: real-time rate measurements of dissolution, corrosion, and passivation, Corrosion 75 (2019) 1398–1419, https://doi.org/10.5006/3336.
[44] S. Cherevko, K.J.J. Mayrhofer, On-line inductively coupled plasma spectrometry in electrochemistry: basic principles and applications, in: K. Wandelt (Ed.), Encyclopedia of Interfacial Chemistry, Elsevier, Oxford, 2018, pp. 326–335.
[45] D. Göhl, H. Rueß, A.M. Mingers, K.J.J. Mayrhofer, J.M. Schneider, M. Ledendecker, Electrochemical passivation properties of valve transition metal carbides, J. Electrochem. Soc. 169 (2022), https://doi.org/10.1149/1945-7111/ac47e6.
[46] J.C. Stinville, P. Villechaise, C. Templier, J.P. Riviere, M. Drouet, Plasma nitriding of 316L austenitic stainless steel: experimental investigation of fatigue life and surface evolution, Surf. Coat. Technol. 204 (2010) 1947–1951, https://doi.org/10.1016/j.surfcoat.2009.09.052.
[47] F. Borgioli, A. Fossati, E. Galvanetto, T. Bacci, G. Pradelli, Glow discharge nitriding of AISI 316L austenitic stainless steel: influence of treatment pressure, Surf. Coat. Technol. 200 (2006) 5505–5513, https://doi.org/10.1016/j.surfcoat.2005.07.073.
[48] M. Pourbaix, Atlas of Electrochemical Equilibria in Aqueous Solutions, National Association of Corrosion Engineers, Houston, 1974.
[49] N.C. Röttcher, G.D. Akkoc, S. Finger, B. Fritsch, J. Möller, K.J.J. Mayrhofer, D. Dworschak, Accelerating materials research with a comprehensive data management tool: a case study on an electrochemical laboratory, J. Mater. Chem. A 12 (2024) 3933–3942, https://doi.org/10.1039/d3ta06247c.
[50] N. Doebelin, R. Kleeberg, Profex: a graphical user interface for the Rietveld refinement program BGMN, J. Appl. Crystallogr. 48 (2015) 1573–1580, https://doi.org/10.1107/S1600576715014685.
[51] W.C. Lenthe, S. Singh, M. Graef, A spherical harmonic transform approach to the indexing of electron back-scattered diffraction patterns, Ultramicroscopy 207 (2019) 112841, https://doi.org/10.1016/j.ultramic.2019.112841.
[52] S. Singh, F. Ram, M. De Graef, EMsoft: open source software for electron diffraction/image simulations, Microsc. Microanal. 23 (2017) 212–213, https://doi.org/10.1017/s143192761700174x.
[53] B. Lynch, Z. Wang, L. Ma, E.-M. Paschalidou, F. Wiame, V. Maurice, P. Marcus, Passivation-induced Cr and Mo enrichments of 316L stainless steel surfaces and effects of controlled pre-oxidation, J. Electrochem. Soc. 167 (2020) 141509, https://doi.org/10.1149/1945-7111/abc727.
[54] E. McCafferty, Introduction to Corrosion Science, Springer, New York, 2010.
[55] Z. Wang, E.-M. Paschalidou, A. Seyeux, S. Zanna, V. Maurice, P. Marcus, Mechanisms of Cr and Mo enrichments in the passive oxide film on 316L austenitic stainless steel, Front. Mater. 6 (2019) 232, https://doi.org/10.3389/fmats.2019.00232.
[56] M.J.K. Lodhi, K.M. Deen, W. Haider, Corrosion behavior of additively manufactured 316L stainless steel in acidic media, Materialia 2 (2018) 111–121, https://doi.org/10.1016/j.mtla.2018.06.015.
[57] S. Choudhary, V. Cruz, A. Pandey, S. Thomas, N. Birbilis, Element-resolved electrochemical analysis of the passivity of additively manufactured stainless steel 316L, Corros. Sci. 189 (2021), https://doi.org/10.1016/j.corsci.2021.109576.
[58] G. Lothongkum, P. Vongbandit, P. Nongluck, Experimental determination of E-pH diagrams for 316L stainless steel in air-saturated aqueous solutions containing 0-5,000 ppm of chloride using a potentiodynamic method, Anti-Corros, Methods Mater 53 (2006) 169–174, https://doi.org/10.1108/00035590610665581.
[59] I. Betova, M. Bojinov, T. Laitinen, K. Mäkelä, P. Pohjanne, T. Saario, The transpassive dissolution mechanism of highly alloyed stainless steels: I. Experimental results and modelling procedure, Corros. Sci. 44 (2002) 2675–2697, https://doi.org/10.1016/S0010-938X(02)00073-2.
[60] A. Fattah-alhosseini, A. Saatchi, M.A. Golozar, K. Raeissi, The transpassive dissolution mechanism of 316L stainless steel, Electrochim. Acta 54 (2009) 3645–3650, https://doi.org/10.1016/j.electacta.2009.01.040.
[61] F. Lu, M. Zhou, Y. Zhou, X. Zeng, First-row transition metal based catalysts for the oxygen evolution reaction under alkaline conditions: basic principles and recent advances, Small 13 (2017) 1701931, https://doi.org/10.1002/smll.201701931.
[62] A. Raza, K.M. Deen, E. Asselin, W. Haider, A review on the electrocatalytic dissociation of water over stainless steel: hydrogen and oxygen evolution reactions, Renew. Sustain. Energy Rev. 161 (2022), https://doi.org/10.1016/j.rser.2022.112323.
[63] F. Yu, F. Li, L. Sun, Stainless steel as an efficient electrocatalyst for water oxidation in alkaline solution, Int. J. Hydrogen Energy 41 (2016) 5230–5233, https://doi.org/10.1016/j.ijhydene.2016.01.108.
[64] O. Kasian, J.P. Grote, S. Geiger, S. Cherevko, K.J.J. Mayrhofer, The common intermediates of oxygen evolution and dissolution reactions during water electrolysis on iridium, Angew Chem. Int. Ed. Engl. 57 (2018) 2488–2491, https://doi.org/10.1002/anie.201709652.
[65] I. Katsounaros, J.C. Meier, S.O. Klemm, A.A. Topalov, P.U. Biedermann, M. Auinger, K.J.J. Mayrhofer, The effective surface pH during reactions at the solid–liquid interface, Electrochem. Commun. 13 (2011) 634–637, https://doi.org/10.1016/j.elecom.2011.03.032.
[66] N. Wiberg, Lehrbuch der Anorganischen Chemie, 102. stark umgearbeitete und verbesserte Auflage, De Gruyter, Berlin, 2008.
[67] H.H. Uhlig, T.L. O'Connor, Nature of the passive film on iron in concentrated nitric acid, J. Electrochem. Soc. 102 (1955) 562, https://doi.org/10.1149/1.2429913.
[68] K.J. Laidler, The development of the Arrhenius equation, J. Chem. Educ. 61 (1984) 494, https://doi.org/10.1021/ed061p494.
[69] S. Czioska, K. Ehelebe, J. Geppert, D. Escalera-López, A. Boubnov, E. Saraçi, B. Mayerhöfer, U. Krewer, S. Cherevko, J.D. Grunwaldt, Heating up the OER: investigation of IrO2 OER catalysts as function of potential and temperature, Chemelectrochem 9 (2022), https://doi.org/10.1002/celc.202200514.
[70] Y. Yang, L. Guo, H. Liu, The effect of temperature on corrosion behavior of SS316L in the cathode environment of proton exchange membrane fuel cells, J. Power Sources 196 (2011) 5503–5510, https://doi.org/10.1016/j.jpowsour.2011.02.070.
[71] J. Xuan, L. Xu, S. Bai, T. Zhao, Y. Xin, G. Zhang, L. Xue, L. Li, Influence of temperature on corrosion behavior, wettability, and surface conductivity of 304 stainless steel in simulated cathode environment of proton exchange membrane fuel cells, Int. J. Hydrogen Energy 46 (2021) 22920–22931, https://doi.org/10.1016/j.ijhydene.2021.04.119.